Electronic Supplementary Material (ESI) for Sustainable Energy & Fuels.

A Li-F co-doped g-C_3N_4/TiO_2-B(001) heterostructure as an efficient hydrogen evolution photocatalyst

Xiaojia Yuan[a], Shuhan Tang[a,b] and Xiaojie Liu[a,b,*]

[a]Center for Quantum Sciences and School of Physics, Northeast Normal University, Changchun, 130117, China.
[b]Center for Advanced Optoelectronic Functional Materials Research, and Key Laboratory of UV Light-Emitting Materials and Technology of Ministry of Educations, Northeast Normal University, Changchun, 130024, China.

Geometries and electronic properties of mono-doped monolayers

In order to explore the influence of Li- or F-doping on the geometry and electronic property of g-C_3N_4 and TiO_2-B(001), the relaxed geometries and partial density of states (PDOS) are presented in Fig. S1-S2. Li atom is located at the center of the hole in g-C_3N_4 monolayer as one can see from Fig. S1(a). It can be seen that strong chemical bonds are formed between the lower electronegative Li atom and higher electronegative and more active N atoms (also called pyridine N). The Li-N bond lengths are 2.10~2.76 Å, as shown in Fig. S1(a). In particular for N15 atom, the interaction between N15 and Li atom is the strongest with the shortest bond length of 2.10 Å. Interestingly, we find the structure of Li-doped g-C_3N_4 is mirror-symmetric, which we can see the blue dash line in Fig. S1(a). With the dash line as the symmetry element, the distribution of Li-N bonds is symmetric. Besides, the strong interaction between Li atom and pyridine N can also be seen from PDOS, which is shown in Fig. S1(b). It can be found that the *s* states of Li atom are noticeably hybridized with the *p* states of pyridine N atoms (i.e., N15, N11 and N12) around -3.0 eV. In addition, it is found that Li-doped g-C_3N_4 will introduce impurity states below the conduction band. The existence of impurity states is unfavorable to the migration of the photoinduced carrier, which leads to the degradation of the photocatalytic performance. These impurity states mainly come from the carbon atoms near the Li atom, especially C12, which we can see from Fig. S1(b). N15 atom, which is pyridine N with higher activity, forms strong chemical bond with Li atom. Thus, its activity is weakened. This is confirmed by the bond length of N15-C12 since the bond length is lengthened from 1.33 to 1.36 Å. While the bond length of N4-C12 is 1.56 Å. According to our previous theory of the bond length-activity relationship,[1] the activity of C12 atom is more affected by N15 than by N4. The lengthened N15-C12 bond makes C12 more active and contributes to the impurity states near the Fermi level. As we mentioned above, these carbons are all symmetrically distributed around the Li atom, thus, their electronic states distributions are similar.

The geometric structure and PDOS of F-doped TiO_2-B(001) are shown in Fig. S2(a)-(b). There are many isomers of F-doped TiO_2-B(001), but according to the surface activity of TiO_2-B(001),[2] the unsaturated Ti, i.e., Ti^*_{5c} (Ti4), is the optimal site for F-doping. This is because Ti^*_{5c} has the lowest electrostatic potential, which can attract F atom. The structure of F-doped TiO_2-B(001) is shown in Fig. S2(a). It is found the length of the F-Ti bond is 1.82 Å. Obviously, they form polar chemical bond. Similar to the case of Li-doped g-C_3N_4, from PDOS, it can also be seen that there is a strong hybridization between the *d* states of Ti atom and the *p* states of F atom below the Fermi level, which again confirms the strong chemical bond between them. The F-doping also introduces some impurity states into the band gap of TiO_2-B(001). After careful analysis, we find that the impurity states above the valence band are mainly contributed by the *p* states of O8 and O18 atoms, while the impurity states below the conduction band are mainly from the *d* states of Ti^{*}_{5c}, which one can see from Fig. S2(b). The activity analysis for O8 and O18 atoms is similar to the analysis of C12 atom mentioned above. The activity of Ti^{*}_{5c} atom decreases because of formation of Ti-F bond. The bond length of O8-Ti^{*}_{5c} is lengthened from 2.11 to 2.23 Å, and the bond length of O18-Ti^{*}_{5c} is lengthened from 1.82 to 2.09 Å. Thus, the activity of O8 and O18 increases and they contribute to the impurity states above the Fermi level.

Geometries of mono-doped and co-doped heterostructures

Li@g-C_3N_4/TiO_2-B(001), g-C_3N_4/F@TiO_2-B(001) and Li@g-C_3N_4/F@TiO_2-B(001) heterostructures are fabricated by supporting g-C_3N_4 or Li@g-C_3N_4 monolayer with TiO_2-B(001) surface or F@TiO_2-B(001) surface, which are showed in Fig. S3. More detailed lattice parameters can be found in our previous research.[3] Compared with the study of F@g-C_3N_4/TiO_2-B(001) heterostructure,[4] Li-F co-doping does not cause significant deformation of the g-C_3N_4 lattice since F is far away from pyridine N in g-C_3N_4. The thicknesses of Li@g-C_3N_4 or g-C_3N_4 monolayer in heterostructures are 0.640 Å, 0.817 Å and 0.763 Å, respectively. Compared with the thickness of g-C_3N_4 monolayer (i.e., 0.858 Å) in g-C_3N_4/TiO_2-B(001) heterostructure,[3] the thicknesses of g-C_3N_4 monolayer in Li@g-C_3N_4/TiO_2-B(001), g-C_3N_4/F@TiO_2-B(001) and Li@g-C_3N_4/F@TiO_2-B(001) heterostructures are reduced, indicating that Li-, F- mono-doping or co-doping can enhance the interlayer interaction between g-C_3N_4 and TiO_2-B(001) layers, which would promote charge transfer at the interface.

Built-in electric field strength

The planar-average electrostatic potential $\overline{V}(z)$ across g-C_3N_4/TiO_2-B(001) and Li@g-C_3N_4/F@TiO_2-B(001) heterostructures is shown in Fig. S4, which is calculated by using following formula:[5]

$$\overline{V}(z) = \frac{1}{A}\int V(\vec{r})dxdy$$

where A is the area of heterostructure interface and V(***r***) is the electrostatic potential of the heterostructures.

It is well known that the built-in electric field plays an important role in the directional movement of photocarrier in the photocatalytic system. In order to identify the built-in electric field at the interface of the heterostructures, we also calculate the electrostatic potential. It has been reported that the electric field distribution can be evaluated by taking the gradient of the electrostatic potentials along the linescan direction, especially for lateral heterostructures.[6-8] However, for the vertical heterostructures, the electrostatic potential distribution due to interlayer interaction is extremely uneven. Strictly speaking, it is difficult to accurately and quantitatively estimate the field strength for a non-uniform electric field[6] because it is position-dependent. In order to qualitatively estimate the field strength, we calculated the average electric field strength of heterostructures from planar-average electrostatic potential. The calculated interlayer distance (d) between g-C_3N_4 monolayer and TiO_2-B(001) surface is 3.59 Å, and planar-average electrostatic potential difference (ΔU) between them is 5.53 V. Thus, the built-in electric field strength in the g-C_3N_4/TiO_2-B(001) is 1.54 V/Å. On the other hand, the calculated interlayer distance (d) between Li@g-C_3N_4 monolayer and F@TiO_2-B(001) surface is 3.76 Å, and planar-average electrostatic potential difference (ΔU) between them is 8.15 V. Therefore, the built-in electric field strength is 2.17 V/Å in Li@g-C_3N_4/F@TiO_2-B(001) heterostructure. The qualitative field strength evaluation implies that the built-in electric field of Li-F co-doped g-C_3N_4/TiO_2-B(001) heterostructure is stronger than that of the undoped g-C_3N_4/TiO_2-B(001) heterostructure. Therefore, the spatial separation efficiency of photoinduced electron-hole pairs in the Li-F co-doped g-C_3N_4/TiO_2-B(001) heterostructure is higher than that of the photoinduced electron-hole pairs in the undoped g-C_3N_4/TiO_2-B(001) heterostructure, under the action of the built-in electric field.

The Gibbs free energy changes (ΔG)

The thermodynamic processes of hydrogen evolution reaction (HER) are examined to estimate the photocatalytic activity of pure g-C_3N_4 monolayer, g-C_3N_4/TiO_2-B(001) heterostructure and Li@g-C_3N_4/F@TiO_2-B(001) heterostructure. The two electrons reaction pathway of HER can be described as:

$$\text{Step 1: } * + H^+ + e^- \rightarrow H* \tag{1}$$

$$\text{Step 2: } H* + H^+ + e^- \rightarrow H_2* \tag{2}$$

where * denotes surface of pure g-C_3N_4 monolayer, g-C_3N_4/TiO_2-B(001) heterostructure or Li@g-C_3N_4/F@TiO_2-B(001) heterostructure, (radical)* denotes the corresponding radical adsorbed on the surface. For step 1 and step 2, each step consumes a proton and an electron. The Gibbs free energy change (ΔG) was calculated according to the study of Skúlason et al.,[9] which is defined as:

$$\Delta G = \Delta E + \Delta E_{zpe} - T\Delta S + \Delta G_U + \Delta G_{pH} \tag{3}$$

where ΔE, ΔE_{zpe} and ΔS are the total energy difference, zero point energy change and energy change in entropy at 298.15 K. ΔG_U is the Gibbs free energy change imposed by external potential U_{red} from photoinduced electrons. ΔG_{pH} refers to the Gibbs free energy change under the influence of pH level. In current study, the Gibbs free energy changes ΔG for every step at pH=0 are obtained through the following equations:

$$\Delta G_1 = E_{H*} - E_* - \frac{1}{2}E_{H_2} - eU_{red} \tag{4}$$

$$\Delta G_2 = E_{H_2*} - E_{H*} - \frac{1}{2}E_{H_2} - eU_{red} \tag{5}$$

where $E_{H^+ + e^-}$ is replaced by $\frac{1}{2}E_{H_2}$, considering the reaction of $H^+ + e^- \rightarrow H_2$ is in equilibrium state at standard condition.

Adsorption of HER intermediates

In order to clarify the ground-state structures of the HER intermediates on various substrates, it is crucial to investigate the active site on the surface of pure g-C_3N_4 monolayer, g-C_3N_4/TiO_2-B(001) heterostructure and Li@g-C_3N_4/F@TiO_2-B(001) heterostructure, respectively. The supercells of pure g-C_3N_4 monolayer, g-C_3N_4/TiO_2-B(001) heterostructure and Li@g-C_3N_4/F@TiO_2-B(001) heterostructure are shown in Fig. S5, in which local active sites are also presented. In our previous study,[4] it was reported that there are two non-equivalent carbon atoms and three non-equivalent nitrogen atoms in pure g-C_3N_4 as one can see from Fig. S5(a). These non-equivalent sites are candidate adsorption sites for HER intermediates. It is well known that N atom, especially for pyridine N, is the optimal adsorption site for the foreign element.

We note that the two "holes" are equivalent in free-standing g-C_3N_4 monolayer. However, the two "holes" are not equivalent in g-C_3N_4/TiO_2-B(001) heterostructure due to the perturbation of TiO_2-B(001) substrate. Therefore, the surface active sites are abundant in g-C_3N_4/TiO_2-B(001) heterostructure, and all candidate adsorption sites of the HER intermediates are labeled in Fig. S5(b). A similar analysis is also performed on Li@g-C_3N_4/F@TiO_2-B(001) heterostructure and the possible adsorption site of the HER intermediates are shown in Fig. S5(c). We should note that although there are two "holes" on the surface of Li@g-C_3N_4/F@TiO_2-B(001) heterostructure, there is strong repulsive interaction for proton due to the existence of Li atom. Therefore, the active sites of the HER intermediates are mainly focused on the N atoms around another hole.

It has been reported that the electrostatic potential can be used to evaluate the surface activity.[2] In addition, the interaction between layers can also influence the activity of the surface atoms in heterostructures. Therefore, electrostatic potential and interlayer distance are investigated to examine the activity of atoms on the surface of g-C_3N_4/TiO_2-B(001) and Li@g-C_3N_4/F@TiO_2-B(001) heterostructures, which are listed in Table S1 and Table S2. In the case of g-C_3N_4/TiO_2-B(001) heterostructure, it can be found that N atoms with lower the electrostatic potential and shorter interlayer distances should be more active than other N atoms. This is because the N atom closer to the substrate of TiO_2-B(001) substrate loses partial electrons due to the interlayer interaction, leading to the reduction of the electrostatic potential of the N atom. Thus, it is easier to trap hydrogen atoms. A similar trend can also be observed in Li@g-C_3N_4/F@TiO_2-B(001) heterostructure. Therefore, we will focus on the adsorption of HER intermediates on N2, N8 and N16, as well as N16 on the surfaces of g-C_3N_4, g-C_3N_4/TiO_2-B(001) as well as Li@g-C_3N_4/F@TiO_2-B(001).

Various possible adsorption configurations of HER intermediates on g-C_3N_4, g-C_3N_4/TiO_2-B(001) and Li@g-C_3N_4/F@TiO_2-B(001) are shown in Fig. S6-S8, respectively. The corresponding Gibbs free energy changes are also shown below each configuration. It can be seen that the Gibbs free energy changes of the first step (ΔG_1) at C1, C2, N1, N2 and N3 sites on g-C_3N_4 monolayer are 0.982, 1.435, -0.175, -0.495 and 1.425 eV, respectively, as one can see from Fig. S6. Therefore, the active site in the first step of the HER on pure g-C_3N_4 monolayer is N2 and this configuration is used for the subsequent adsorption of the second proton. The second step of HER on pure g-C_3N_4 is shown in Fig. S6(f)-(j). As for these three possible adsorption modes of H_2/g-C_3N_4, i.e. H*+H*, H*H* and H_2*, the Gibbs free energy changes (ΔG_2) of the most stable structure is 0.743, 1.271 and 0.470 eV, respectively. For the HER intermediates on g-C_3N_4/TiO_2-B(001), there are more than a dozen adsorption configurations, which are shown in Fig. S7. Among these isomers of H/g-C_3N_4/TiO_2-B(001), it is found N8 and N16 sites are the more stable adsorption configurations. The Gibbs free energy changes of the first step on N8 and N16 sites are -0.585 eV and -0.586 eV, respectively. The most stable configuration (N16) is also used for the subsequent HER process analysis as shown in Fig. S7(m)-(o). Finally, in the case of Li@g-C_3N_4/F@TiO_2-B(001) heterostructure, it is found that N16 site is the best adsorption site because the Gibbs free energy change is the lowest with the values of -0.646 eV. Therefore, N16 site is the H^+ adsorption site for the first step in HER for Li@g-C_3N_4/F@TiO_2-B(001) heterostructure, which is also used for the subsequent proton adsorption in Fig. S8(f)-(h). Other adsorption configurations of the HER intermediates as shown in Fig. S8(a)-(d) are not competitive since their Gibbs free energy changes are relatively higher.

Optical absorption spectra

Optical absorption coefficient is an important parameter to evaluate the utilization efficiency of photocatalysts for sunlight. The absorption coefficient I(ω) is obtained based on the following equation:[10]

$$I(\omega)=\frac{\sqrt{2}\omega}{c}(\sqrt{\varepsilon_1^2+\varepsilon_2^2}-\varepsilon_1)^{\frac{1}{2}} \tag{6}$$

where ε_1 and ε_2 are the real and imaginary parts of the dielectric function, and ω is the photon frequency. The imaginary part of the dielectric function is obtained from the following equation:[11]

$$\varepsilon_2(\omega)=\frac{4\pi^2e^2}{\Omega}\lim_{q\to 0}\frac{1}{q^2}\times\sum_{c,v,\vec{k}}2w_{\vec{k}}\delta(E_c-E_v-E_\omega)\times\left\langle u_{c\vec{k}+e_\alpha q}\middle|u_{v\vec{k}}\right\rangle\left\langle u_{c\vec{k}+e_\beta q}\middle|u_{v\vec{k}}\right\rangle^* \tag{7}$$

The real part of the dielectric function ε_1 can be determined from the Kramers-Kronig transform given by:[12]

$$\varepsilon_1(\omega)=1+\frac{2}{\pi}P\int_0^\infty\frac{\varepsilon_2(\omega')\omega'}{\omega'^2-\omega^2}d\omega' \tag{8}$$

where P denotes the principle value and η is the complex shift parameter. Although dielectric function exhibits tensor nature, the optical absorption is dominated by the in-plane absorption component $I_{//}(\omega)$, whereas the contribution of the out-plane absorption component $I_\perp(\omega)$ is negligible.

The optical absorption spectra of isolated g-C_3N_4, Li@g-C_3N_4, TiO_2-B(001), F@TiO_2-B(001) and Li@g-C_3N_4/F@TiO_2-B(001) heterostructure are shown in Fig. S9. As we can see, pure g-C_3N_4 monolayer and TiO_2-B(001) surface can be excited only by ultraviolet light and partial amount of visible light. After F-doping, the optical absorption spectrum of F@TiO_2-B(001) surface begins to red shift as one can see solid olive line. It is worth noting that the absorption response of Li@g-C_3N_4/F@TiO_2-B(001) heterostructure has been widened. It exhibits strongest absorption intensity in the visible light region due to its narrowed band gap. In order to quantify the UV absorption intensity, the integration of the absorption spectra has been investigated, and the integrated intensity in ultraviolet region of the isolated g-C_3N_4, TiO_2-B(001), Li@g-C_3N_4, F@TiO_2-B(001) and Li@g-C_3N_4/F@TiO_2-B(001) heterostructure are $0.76´10^8$, $1.24´10^8$, $0.70´10^8$, $1.09´10^8$ and $1.31´10^8$, respectively. It can be found that for g-C_3N_4 and TiO_2-B(001) surfaces, the UV absorption intensity of the Li-doping and F-doping system is not significant increased. But the UV adsorption intensity of the co-doped Li@g-C_3N_4/F@TiO_2-B(001) heterostructure gets more enhanced than the others.

References

[1] X. Yuan, S. Qiu and X. Liu, *J. Solid State Chem.*, 2022, **315**, 123480.

[2] W. Yan, X. Yuan and X. Liu, *Appl. Surf. Sci.*, 2019, **494**, 850-858.

[3] X. Yuan and X. Liu, *Phys. Chem. Chem. Phys.*, 2022, **24**, 17703.

[4] X. Yuan, S. Tang, S. Qiu and X. Liu, *J. Phys. Chem. C*, 2023, **127**, 1828-1840.

[5] M. Peressi, N. Binggeli and A. Baldereschi, *J. Phys. D: Appl. Phys.*, 1998, **31**, 1273-1299.

[6] J. Tian, K. Lu and X. Liu, *Appl. Surf. Sci.*, 2022, **599**, 154057.

[7] X. Liu, C.-Z. Wang, M. Hupalo, H.-Q. Lin, K.-M. Ho and M. C. Tringides, *Phys. Rev. B*, 2014, **89**, 041401.

[8] C. Du, L. Yu, X. Liu, L. Liu and C.-Z. Wan, *Sci. Rep.*, 2017, **7**, 13152.

[9] E. Skúlason, G. S. Karlberg, J. Rossmeisl, T. Bligaard, J. Greeley, Hannes Jónsson and J. K. Nørskov, *Phys. Chem. Chem. Phys.*, 2007, **9**, 3241-3250.

[10] P. Ravindran, A. Delin, B. Johansson and O. Eriksson, *Phys. Rev. B*, 1999, **53**, 1776-1785.

[11] M. Gajdoš, K. Hummer and G. Kresse, *Phys. Rev. B*, 2006, **73**, 045112.

Table S1. Electrostatic potential at 2 Å above the N atoms in g-C_3N_4/TiO_2-B(001) heterostructure, distance interlayer (d) between N atoms and TiO_2-B(001) surface in g-C_3N_4/TiO_2-B(001) heterostructure and Gibbs free energy changes of H/g-C_3N_4/TiO_2-B(001) at different adsorption sites.

N atoms	**Electrostatic potential (V)**	**d (Å)**	**ΔG_1 (eV)**
N2	2.880	3.82	-0.494
N3	3.083	3.83	-0.439
N11	2.452	3.02	-0.559
N12	2.844	3.80	-0.494
N14	2.374	3.03	-0.558
N15	3.088	3.82	-0.438
N5	2.926	3.85	—
N6	3.113	3.80	—
N8	2.551	3.22	-0.585
N9	2.946	3.87	—
N13	3.035	3.82	—
N16	**2.522**	**3.21**	**-0.586**
N5	2.926	3.85	—

Table S2. Electrostatic potential at 2 Å above the typical N atoms in Li@g-C_3N_4/F@TiO_2-B(001) heterostructure, distance interlayer (d) between typical N atoms and TiO_2-B(001) surface in Li@g-C_3N_4/F@TiO_2-B(001) heterostructure and Gibbs free energy changes of H/Li@g-C_3N_4/F@TiO_2-B(001) heterostructure at different adsorption sites.

site	Electrostatic potential (V)	d (Å)	ΔG_1 (eV)
N16	1.948	3.33	-0.646
N8	1.949	3.30	-0.610
N9	2.338	4.05	-0.545
N13	2.443	4.04	-0.456

Figure Captions

Fig. S1. (a)-(b) Geometry and partial density of states for Li@g-C_3N_4 monolayer. Bond length of Li-N and C-N bonds (in blue) and the representative atoms (in black) are also shown in **Fig. S1(a)**. The blue dash line is the line symmetry element, representing the mirror symmetry.

Fig. S2. (a)-(b) Geometry and partial density of states for F@TiO_2-B(001) surface. Bond length of F-Ti and O-Ti bonds (in blue) and the representative atoms (in black) are also shown in **Fig. S2(a)**.

Fig. S3. (a)-(b) Geometry of Li@g-C_3N_4/TiO_2-B(001) heterostructure with top and side views. (c)-(d) Geometry of g-C_3N_4/F@TiO_2-B(001) heterostructure with top and side views. (e)-(f) Geometry of Li@g-C_3N_4/F@TiO_2-B(001) heterostructure with top and side views.

Fig. S4. Planar-average electrostatic potential and electric field strength of built-in electric field (E) for (a) g-C_3N_4/TiO_2-B(001) heterostructure and (b) Li@g-C_3N_4/F@TiO_2-B(001) heterostructure.

Fig. S5. (a) Geometry and different kinds of N and C atoms in g-C_3N_4 monolayer. (b) Geometry and label for different N atoms in g-C_3N_4/TiO_2-B(001) heterostructure. (c) Geometry and label for typical N atoms in Li@g-C_3N_4/F@TiO_2-B(001) heterostructure.

Fig. S6. (a)-(e) Geometries and the corresponding Gibbs free energy changes of H/g-C_3N_4 at different adsorption sites. (f)-(j) Geometries and the corresponding Gibbs free energy changes of H_2/g-C_3N_4 at different adsorption sites.

Fig. S7. (a)-(l) Geometries and the corresponding Gibbs free energy changes of H/g-C_3N_4/TiO_2-B(001) heterostructure at different adsorption sites. (m)-(o) Geometries and the corresponding Gibbs free energy changes of H_2/g-C_3N_4/TiO_2-B(001) heterostructure at different adsorption sites.

Fig. S8. (a)-(e) Geometries and the corresponding Gibbs free energy changes of H/Li@g-C_3N_4/F@TiO_2-B(001) heterostructure at different adsorption sites. (f)-(h) Geometries and the corresponding Gibbs free energy changes of H_2/Li@g-C_3N_4/F@TiO_2-B(001) heterostructure at different adsorption sites.

Fig. S9. (a) The optical absorption spectra of the isolated g-C_3N_4, TiO_2-B(001), Li@g-C_3N_4, F@TiO_2-B(001) and Li@g-C_3N_4/F@TiO_2-B(001) heterostructure, respectively. (b) The optical absorption spectra of the isolated g-C_3N_4, TiO_2-B(001), Li@g-C_3N_4, F@TiO_2-B(001) and Li@g-C_3N_4/F@TiO_2-B(001) heterostructure in ultraviolet region, respectively.

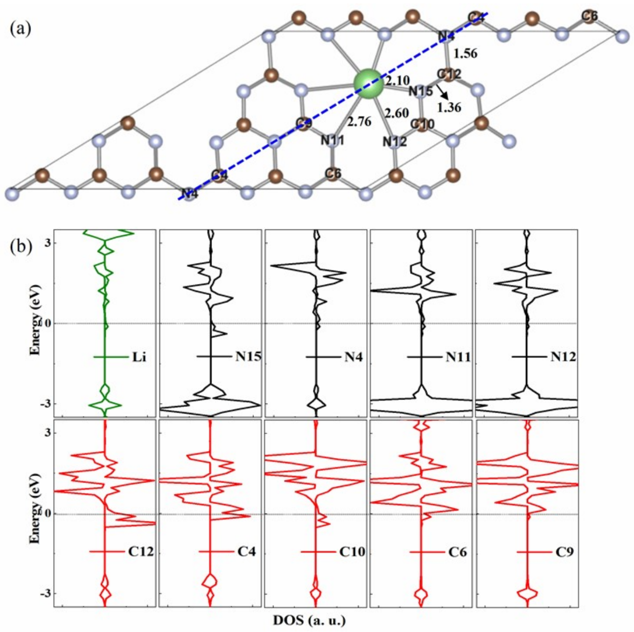

Fig. S1. Geometry and partial density of states for Li@g-C_3N_4 monolayer. Bond length of Li-N and C-N bonds (in blue) and the representative atoms (in black) are also shown in **Fig. S1(a)**. The blue dash line is the line symmetry element, representing the mirror symmetry.

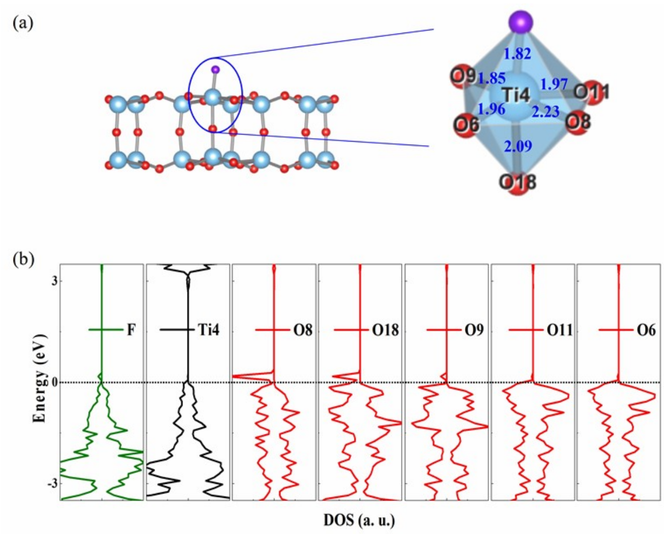

Fig. S2. (a)-(b) Geometry and partial density of states for F@TiO_2-B(001) surface. Bond length of F-Ti and O-Ti bonds (in blue) and the representative atoms (in black) are also shown in **Fig. S2(a)**.

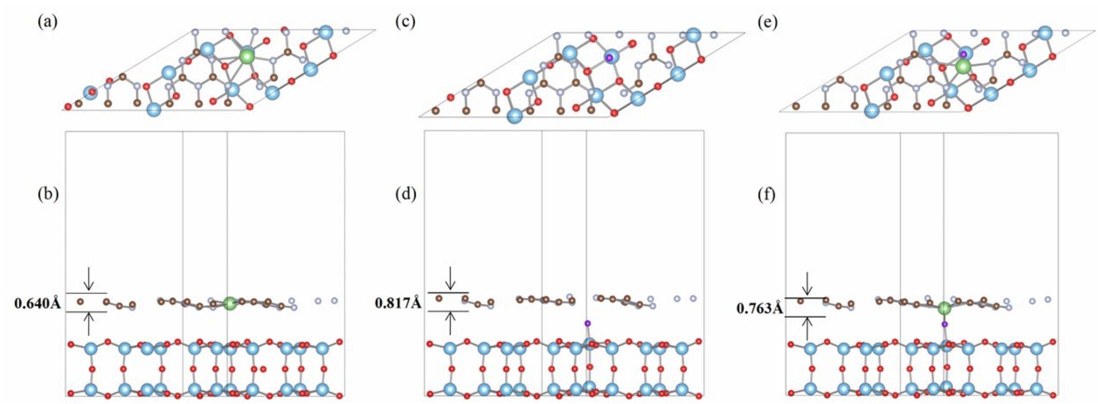

Fig. S3. (a)-(b) Geometry of Li@g-C_3N_4/TiO_2-B(001) heterostructure with top and side views. (c)-(d) Geometry of g-C_3N_4/F@TiO_2-B(001) heterostructure with top and side views. (e)-(f) Geometry of Li@g-C_3N_4/F@TiO_2-B(001) heterostructure with top and side views.

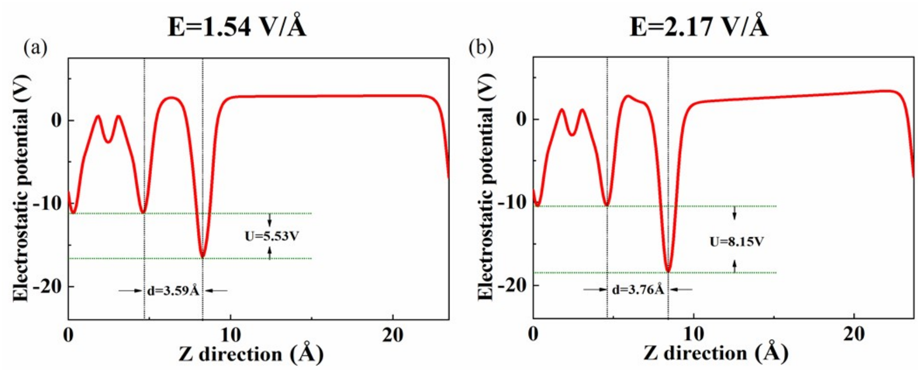

Fig. S4. Planar-average electrostatic potential and electric field strength of built-in electric field (E) for (a) g-C_3N_4/TiO_2-B(001) heterostructure and (b) Li@g-C_3N_4/F@TiO_2-B(001) heterostructure.

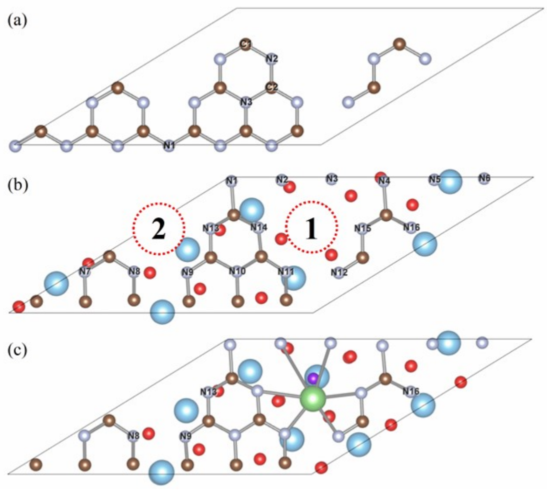

Fig. S5. (a) Geometry and different kinds of N and C atoms in g-C_3N_4 monolayer. (b) Geometry and label for different N atoms in g-C_3N_4/TiO_2-B(001) heterostructure. (c) Geometry and label for typical N atoms in Li@g-C_3N_4/F@TiO_2-B(001) heterostructure.

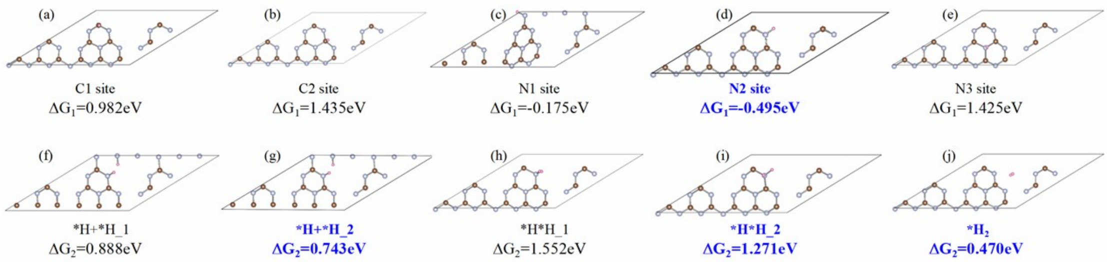

Fig. S6. (a)-(e) Geometries and the corresponding Gibbs free energy changes of H/g-C_3N_4 at different adsorption sites. (f)-(j) Geometries and the corresponding Gibbs free energy changes of H_2/g-C_3N_4 at different adsorption sites.

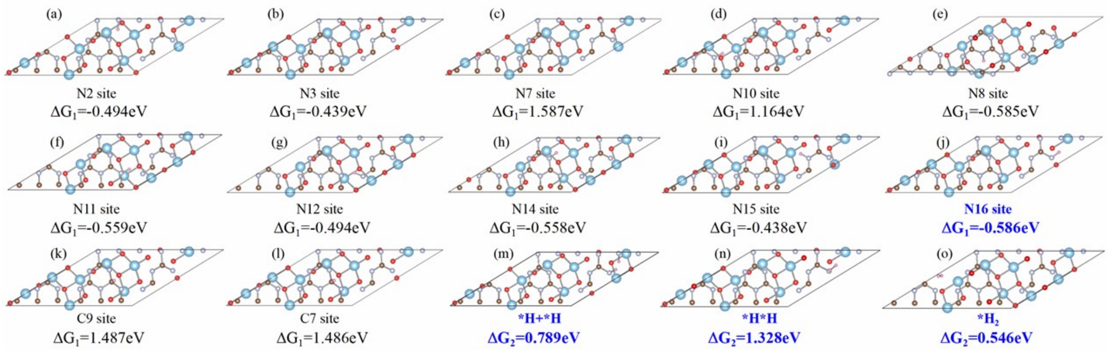

Fig. S7. (a)-(l) Geometries and the corresponding Gibbs free energy changes of H/g-C_3N_4/TiO_2-B(001) heterostructure at different adsorption sites. (m)-(o) Geometries and the corresponding Gibbs free energy changes of H_2/g-C_3N_4/TiO_2-B(001) heterostructure at different adsorption sites.

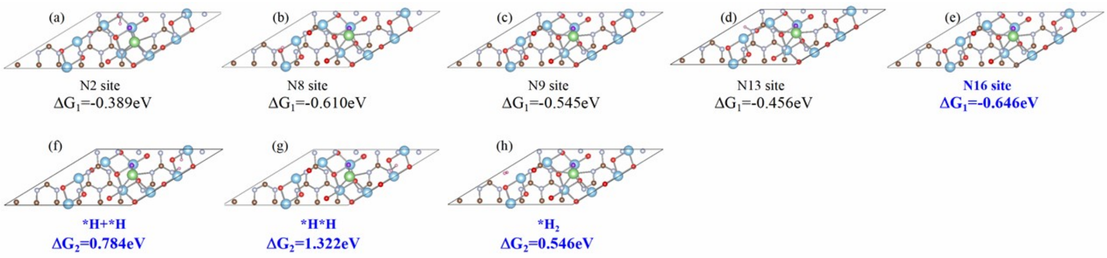

Fig. S8. (a)-(e) Geometries and the corresponding Gibbs free energy changes of H/Li@g-C_3N_4/F@TiO_2-B(001) heterostructure at different adsorption sites. (f)-(h) Geometries and the corresponding Gibbs free energy changes of H_2/Li@g-C_3N_4/F@TiO_2-B(001) heterostructure at different adsorption sites.

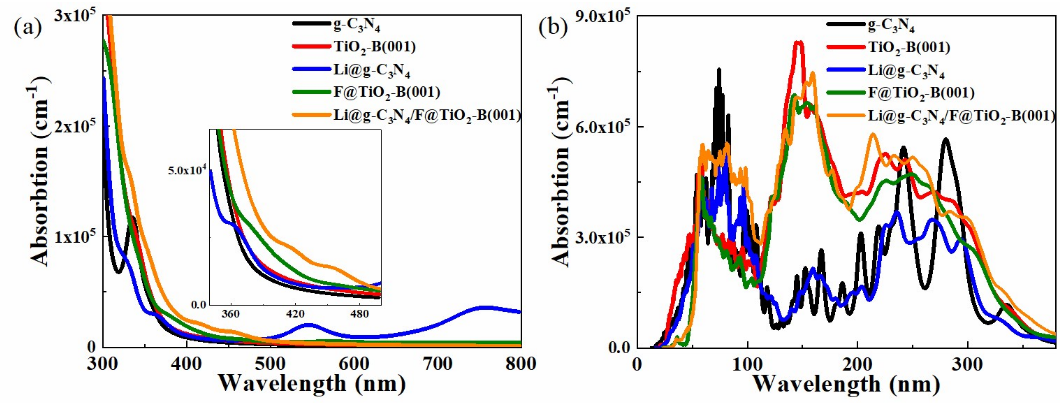

Fig. S9. (a) The optical absorption spectra of the isolated g-C_3N_4, TiO_2-B(001), Li@g-C_3N_4, F@TiO_2-B(001) and Li@g-C_3N_4/F@TiO_2-B(001) heterostructure, respectively. (b) The optical absorption spectra of the isolated g-C_3N_4, TiO_2-B(001), Li@g-C_3N_4, F@TiO_2-B(001) and Li@g-C_3N_4/F@TiO_2-B(001) heterostructure in ultraviolet region, respectively.